A Non-parametric Factor Representation and Editing for Measured Anisotropic Spectral BRDFs

Kei Iwasaki
kiwasaki@mail.saitama-u.ac.jp
Saitama University/Prometech CG Research
Japan

Yoshinori Dobashi
doba@ime.ist.hokudai.ac.jp
Hokkaido University/Prometech CG Research
Japan

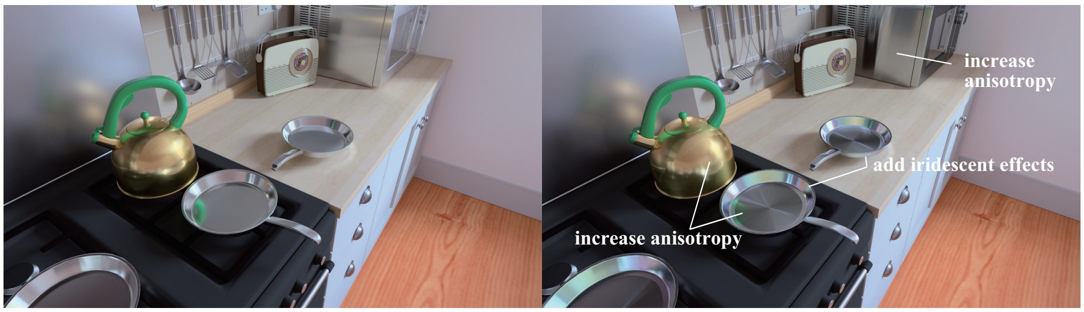

Figure 1: Kitchen scene with the original BRDFs (left) and our non-parametric factor representation of measured anisotropic spectral BRDFs (right). Our representation enables us to edit the normal distribution function and Fresnel terms. Surface materials of the kettle, the frying pans, and the microwave are edited to increase anisotropy, and iridescent effects are added to the surfaces of the frying pans.

ABSTRACT

Measured bidirectional reflectance distribution functions (BRDFs) can accurately represent the measured material appearance but suffer from high storage costs and lack editability due to their high dimensionality. Recent advances in efficient acquisition techniques extend the dimensionality of measured BRDFs from 3D (isotropic) to 4D (anisotropic) and from RGB to spectra. This, however, further compounds the issues of measured BRDFs and limits their practical use. This paper proposes a non-parametric factor representation for measured anisotropic spectral BRDFs. Based on microfacet theory, our method decomposes 4D measured anisotropic BRDF per spectrum into low-dimensional, editable factors. We further compress the spectral domain of decomposed factors using principal component analysis. Experimental results show that our method can compress measured anisotropic spectral BRDFs 1/40 on average and up to 1/333. Our method also provides several editing tools for each factor to enhance the editability of measured anisotropic spectral BRDFs.

CCS CONCEPTS

• **Computing methodologies → Reflectance modeling**.

Conference acronym 'XX, June 03–05, 2018, Woodstock, NY

ACM ISBN 978-1-4503-XXXX-X/18/06
https://doi.org/XXXXXXX.XXXXXXX

KEYWORDS

Anisotropic Spectral BRDF, Non-Parametric Factor Representation, Editing

ACM Reference Format:
Kei Iwasaki and Yoshinori Dobashi. 2018. A Non-parametric Factor Representation and Editing for Measured Anisotropic Spectral BRDFs. In *Proceedings of Make sure to enter the correct conference title from your rights confirmation emai (Conference acronym 'XX)*. ACM, New York, NY, USA, 10 pages. https://doi.org/XXXXXXX.XXXXXXX

1 INTRODUCTION

Data-driven representation of Bidirectional Reflectance Distribution Function (BRDF), which uses measured surface reflectance of real-world materials, can reproduce the material appearance faithfully. In recent years, film productions have started to shift from RGB rendering to spectral rendering. This facilitates the use of spectral BRDFs, and an efficient acquisition method of spectral reflectances of real-world materials has been proposed [12]. While measured spectral BRDFs can reproduce the material appearance faithfully, their data size, especially for anisotropic materials, is prohibitive due to its high dimensionality (four dimension for the directional domain and one dimension for the spectral domain).

In addition, raw measured data can be used only to represent the measured material itself. Thus the expressible range of measured BRDFs is limited to the number of measured materials. Increasing the number of measured materials is not accessible due to the expensive acquisition time, which requires 2-3 days per anisotropic material [12]. Therefore, *compact representation* and *editability* are essential to enhance the practicality of measured anisotropic spectral BRDFs.

Recent approaches representing measured BRDFs with neural networks can faithfully reproduce the original measured BRDFs using low-dimensional latent vectors [13, 17, 32, 36]. While these neural-based models can compactly represent BRDFs, the *entangled* representation makes it difficult to edit measured BRDFs intuitively. Currently, the primary editing tool of these neural-based approaches is interpolating two latent vectors representing two different BRDFs. Interpolating two different BRDFs, while functional, can change the *entire* visual appearance, and it is difficult to edit one property (e.g., shapes and intensities of specular highlight) without changing other properties (e.g., the color of the entire material).

Another common approach to compact representation of measured BRDFs is to decompose into low-dimensional factors [2, 18, 20]. While these methods can repsesent measured BRDFs with low-dimensional, editable factors, these methods are limited to isotropic BRDFs with RGB channels.

This paper proposes a simple but efficient, easy to edit representation for measured anisotropic spectral BRDFs using non-parametric factorization. Based on the microfacet theory, our method decomposes four-dimensional anisotropic reflectance distribution per spectrum into the product of normal distribution function (NDF), Fresnel term, and geometric attenuation factor (GAF), which are stored in a low-dimensional table. Our technical contribution lies in deriving a proper weight for anisotropic BRDFs used to fit BRDFs with non-parametric factors. Since NDFs and GAFs primarily depend on the geometric structures of microfacets, NDFs and GAFs across different spectra can be compactly represented using Principal Component Analysis. Several experiments show that our method can compress five-dimensional measured anisotropic spectral BRDFs about 1/40 on average and up to 1/333 while retaining appearance fidelity as shown in Fig. 1. We also provide several editing tools to enhance the expressiveness of the measured anisotropic spectral BRDFs. Fig. 1 shows an example of editing measured anisotropic spectral BRDFs. Our representation enables us to edit NDFs of the kettle, the frying pans, and the microwave to increase anisotropy, as shown in Fig. 1 bottom. Our representation also naturally fits into the edition of wavelength-dependent effects, such as iridescent effects added to the frying pans, as shown in Fig. 1.

2 PREVIOUS WORK

2.1 Measured BRDFs

Matusik et al. measured the surface reflectances of real-world isotropic materials for the densely sampled incident and outgoing directions [23]. The publicized dataset referred to as MERL BRDF has been pervasively used in both graphics and vision communities. Filip and Vavra acquired surface reflectances of anisotropic materials (e.g., fabrics) [14]. Dupuy and Jakob proposed an efficient acquisition method of isotropic and anisotropic spectral BRDFs [12]. In this paper, we refer to them as EPFL BRDF.

Although these measured BRDFs can accurately represent real-world materials, measured BRDFs require a large amount of tabulated data, are difficult to edit, and require a costly acquisition process, while several methods [21, 25] have been proposed to reduce the number of acquisition samples. For instance, a single anisotropic material in EPFL BRDF still requires more than 110MB, although it is adaptively sampled.

Several methods have been proposed to edit measured BRDFs [29, 30]. These methods provide intuitive BRDF editing tools by embedding measured BRDFs into low-dimensional space and interpolating them. Our method further enriches editing tools for measured BRDFs, such as editing anisotropy of normal distribution function and editing Fresnel term.

2.2 Parametric Representation of Measured BRDFs

Ngan et al. [24] conducted extensive experiments of fitting MERL BRDFs with parametric BRDF models such as Blinn-Phong [8] and Cook-Torrance [10]. Several methods have been proposed to increase the fitting accuracy of MERL BRDFs by using shifted-Gamma distribution [3], ABC model [22], rational functions [26], fitting roughness parameters using power iteration [11], two-scale microfacet reflectance model [16], image-based adaptive fitting [6]. The expressiveness of these methods is limited to those of underlying parametric models. Moreover, all these methods are adapted to RGB BRDFs, not to spectral BRDFs.

2.3 Non-parametric Representation of Measured BRDFs

Several methods have been proposed to represent BRDFs with lower dimensional factors using singular value decomposition [18], non-negative matrix factorization [20], inverse shade trees [19], tensor decomposition [7], and PCA with logarithmic mapping [25]. These methods do not consider the underlying theory (e.g., microfacet theory) of BRDFs when factoring, resulting in inferior results.

Bagher et al. factored MERL BRDFs into NDF, Fresnel term, and GAF by solving weighted least squares [2]. Sun et al. separated MERL BRDFs into diffuse and specular components [31]. Tongbuasirilai et al. represented isotropic measured BRDFs with a product of one-dimensional factors using the projected deviation vector parameterization [34], and a sparse combination of multi-dimensional dictionaries [33]. While these methods can represent measured BRDFs in a compact fashion with high fidelity, all these methods are limited to isotropic BRDFs with RGB channels. The most relevant work to our method is Bagher's method [2]. The technical contributions of our method against this previous work lie in two folds. Our method extends the previous method to handle anisotropic BRDFs by deriving new weights tailored to anisotropic BRDFs. Furthermore, by analyzing the fitted NDFs and GAFs, and exploiting the similarities of these distributions across different wavelengths, we compress these factors in the spectral domain, while the previous method, which is limited to RGB channels, does not utilize such similarities.

2.4 Neural Representation of Measured BRDFs

Sztrajman et al. represented a measured BRDF with a neural network called Neural BRDF (NBRDF) [32]. NBRDF is represented with a 675D vector corresponding to the neural network weights. NBRDF is further encoded into a 32D latent vector, which is used to interpolate two different materials. Zheng et al. introduced Neural Processes to represent measured BRDFs [36]. Chen et al. proposed invertible BRDF for inverse rendering [9]. Fan et al. represented BRDFs with a latent vector to describe layered BRDFs [13].

While neural-based methods can represent measured BRDFs with low-dimensional latent vectors, those representations are entangled, and these methods edit measured BRDFs by interpolating two latent vectors representing two different BRDFs, which would sometimes generate BRDFs of physically meaningless materials (e.g., interpolating fabrics and metals). On the contrary, our method extracts physically-based meaningful components (i.e., diffuse/specular coefficients, NDF, Fresnel term, and GAF), most of which are orthogonal and easy to edit intuitively.

Hu et al. proposed DeepBRDF that encodes measured BRDFs into latent vectors using an autoencoder [17]. The latent vectors are further mapped onto attribute vectors (corresponding to diffuse/specular albedo and roughness) to edit BRDFs at the cost of an additional network. Benamira et al. proposed an interpretable disentangled parameterization of measured BRDFs using a β-Variational AutoEncoder [5]. While these methods struggle to disentangle the latent space, most of the neural-based methods (except for NBRDF [32]) are limited to isotropic BRDFs. Moreover, all these neural-based methods focus on RGB BRDFs and no methods have been proposed for spectral BRDFs.

3 PROPOSED METHOD

3.1 Anisotropic Fitting Model

Our method represents measured anisotropic spectral BRDFs ρ with the following anisotropic microfacet model ρ_M for each wavelength λ (we omit λ for brevity):

$$\rho_M(\theta_h, \phi_h, \theta_d, \phi_d) = \rho_d + \rho_s \frac{D(\theta_h, \phi_h)F(\theta_d)G(\theta_i, \phi_i)G(\theta_o, \phi_o)}{\cos\theta_i \cos\theta_o}, \tag{1}$$

where ρ_d and ρ_s are the diffuse/specular coefficients, D is the normal distribution function (NDF), F is the Fresnel term, G is the geometric attenuation factor (GAF), respectively. The anisotropic microfacet model ρ_M is parameterized by Rusinkiewicz parameterization [28] $(\theta_h, \phi_h, \theta_d, \phi_d)$, where (θ_h, ϕ_h) are the zenith angle and the azimuthal angle of the half vector $\mathbf{h} = \frac{\mathbf{i}+\mathbf{o}}{\|\mathbf{i}+\mathbf{o}\|}$, $\mathbf{i}$ and $\mathbf{o}$ are the incident and outgoing directions, and (θ_d, ϕ_d) are those of the difference vector $\mathbf{d}$, respectively.

In non-parametric factor representation, NDF D and GAF G are represented by two-dimensional arrays for discretized angles (θ_h, ϕ_h) and (θ, ϕ), and the Fresnel term F is represented with a one-dimensional array for discretized angles θ_d. To better capture important features of NDF D near $\theta_h = 0$, the non-linear mapping of $\theta'_h = \sqrt{\theta_h}$ is used for NDF D similar to the previous methods [2, 12, 23].

Our method calculates ρ_d, ρ_s, D, F, and G by minimizing the following objective function E:

$$E = \sum_j w_j(\rho_j - \rho_M(\mathbf{\Theta}_j))^2, \tag{2}$$

here $\mathbf{\Theta}_j = (\theta'_{h,j}, \phi_{h,j}, \theta_{d,j}, \phi_{d,j})$ is the j-th set of uniformly sampled angles, ρ_j is the measured BRDF value at Θ_j, w_j is a weight for ρ_j described in Sec. 3.2. The objective function E is minimized by using alternating weighted least square method [2], described in Sec. 3.3.

Table 1: Comparisons of the average MAPE, relMSE, PSNR, and SSIM between Bagher's weight and our weight in Fig. 2 for all anisotropic materials. Our weight can significantly reduce the relMSE.

	MAPE↓	relMSE↓	PSNR↑	SSIM↑
Bagher's weight	48.90%	2.3593	44.31	0.9797
our weight	11.03%	0.0483	45.08	0.9878

3.2 Weights for Anisotropic BRDFs

Weight w_j for the measured BRDF ρ_j corresponding to j-th angle set Θ_j consists of three sub-weights, volume form sub-weight w_V, BRDF importance sub-weight w_I, and compressive sub-weight w_C as:

$$w_j = w_V(\Theta_j)w_I(\Theta_j)w_C(\rho_j). \tag{3}$$

Since BRDF importance sub-weight w_I and compressive sub-weight w_C are identical for both isotropic and anisotropic BRDFs, we focus on the volume form sub-weight w_V. w_I and w_C are described in Appendix A. Volume form sub-weight w_V considers the Jacobian of the transformation from the canonical form $(\mathbf{i}, \mathbf{o})$ to Rusinkiewicz parameterization $(\theta_h, \phi_h, \theta_d, \phi_d)$. While the previous method derived the volume form sub-weight w_V for three-angle parameterization $(\theta_h, \theta_d, \phi_d)$ limited to isotropic BRDFs [2], we derive w_V for full parameterization $(\theta_h, \phi_h, \theta_d, \phi_d)$ for anisotropic BRDFs as:

$$w_V = 4\sin\theta_d \sin\theta_h \cos\theta_d d\theta_h d\theta_d d\phi_h d\phi_d. \tag{4}$$

The derivations of the transformation matrix and its Jacobian are shown in the supplemental material. Since Θ_j is uniformly sampled for θ'_h, $d\theta_h = 2\sqrt{\theta_h} d\theta'_h$ is used in *Eq.* (4).

Fig. 2 shows comparisons between Bagher's weight and ours in Eq. (4). As shown in Fig. 2, the use of our weight (second row) can reconstruct the original BRDFs (top row) well, while Bagher's weight (fourth row) leads to visible artifacts, especially for copper_sheet, metallic_paper_copper, metallic_paper_gold, miro_7 materials. Table 1 shows comparisons between our weight and Bagher's weight in terms of image quality metrics, mean absolute percentage error (MAPE), relative mean square error (relMSE), peak signal-to-noise ratio (PSNR), and structural similarity index measure (SSIM). As shown in Fig. 2 and Table 1, our weight tailored to anisotropic BRDFs outperformes Bagher's weight qualitatively and quantitatively, as indicated by MAPE and relMSE.

3.3 Fitting Procedure using AWLS

To fit each component of NDF D, Fresnel term F, GAF G, our method solves the objective function E in Eq. (2) using alternating weighted least squares (AWLS) [2]. Let us explain the fitting procedure of the Fresnel term $F(\theta_d, \lambda)$ for each sampled wavelength λ. In the following explanation, we omit λ for clarification and the following procedure is repeated for all sampled wavelengths.

Fresnel term F is represented with $\mathbf{F} \in \mathbb{R}^{N_d}$, where θ_d is discretized into N_d angles. To obtain $\mathbf{F}$ using AWLS, other factors

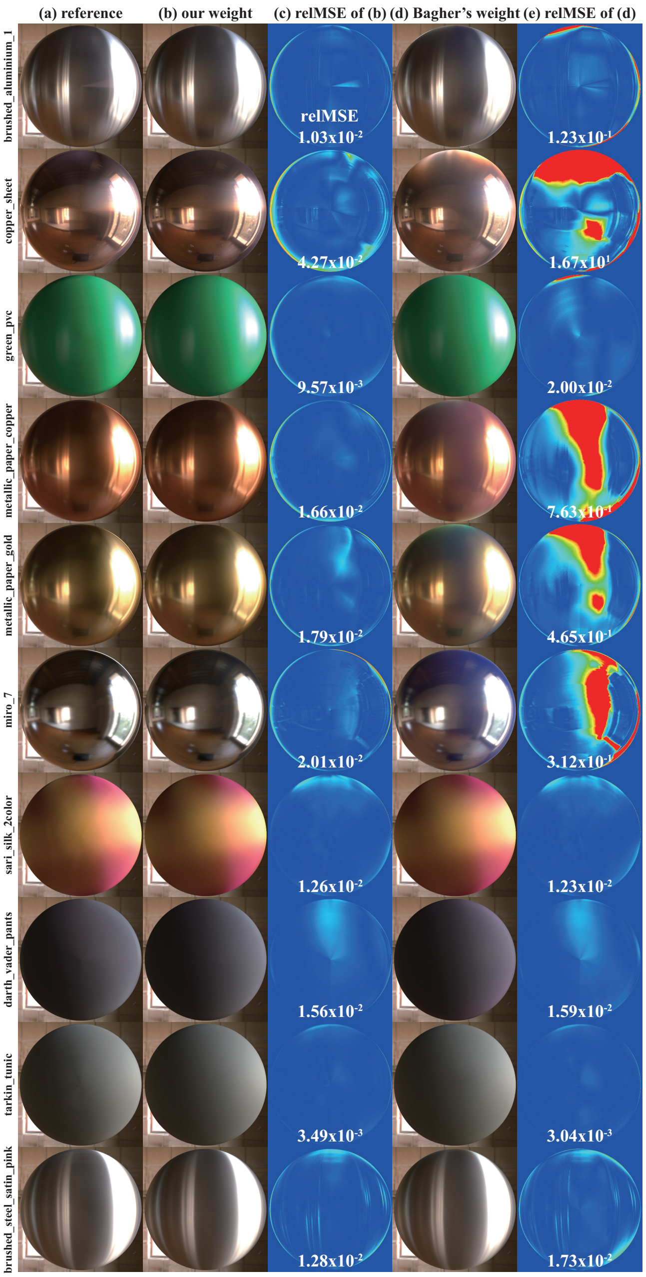

Figure 2: Comparisons between (b) our weight tailored to anisotropic BRDFs and (d) Bagher's weight. (a) reference images rendered with original BRDFs, (b) rendering results using our weights in Eq. (4), (c) visualization of relative mean square error (relMSE) of (b), (d) rendering results using Bagher's weight, (e) relMSE of (d). Artifacts due to the use of three-angle parametrization volume form sub-weight can be seen in copper_sheet, metallic_paper_copper, metallic_paper_gold, and miro_7 materials.

ρ_d, ρ_s, D and G are considered as constant. To compute the k-th component f_k of $\mathbf{F}$, the objective function E with respect to f_k is rewritten as:

$$E(f_k) = \sum_{j \in I_k} w_j (a_j - b_j f_k)^2, \tag{5}$$

$$a_j = \rho_j - \rho_d, \tag{6}$$

$$b_j = \frac{\rho_s D(\theta_{h,j}, \phi_{h,j}) G(\theta_{i,j}, \phi_{i,j}) G(\theta_{o,j}, \phi_{o,j})}{\cos\theta_{i,j} \cos\theta_{o,j}}, \tag{7}$$

where ρ_j is the measured BRDF value of $(\theta_{h,j}, \phi_{h,j}, \theta_{d,j}, \phi_{d,j})$, I_k is the set of indices of uniformly sampled Rusinkiewicz parameterization angles Θ whose θ_d is equal to the k-th discretized angle. $\cos\theta_{i,j}$ and $\cos\theta_{o,j}$ are calculated as:

$$\cos\theta_{i,j} = \cos\theta_{h,j} \cos\theta_{d,j} - \sin\theta_{h,j} \sin\theta_{d,j} \cos\phi_{d,j}, \tag{8}$$

$$\cos\theta_{o,j} = \cos\theta_{h,j} \cos\theta_{d,j} + \sin\theta_{h,j} \sin\theta_{d,j} \cos\phi_{d,j}. \tag{9}$$

Then f_k is simply calculated as:

$$f_k = \frac{\sum_{j \in I_k} w_j a_j b_j}{\sum_{j \in I_k} w_j b_j^2}. \tag{10}$$

Other factors D, G, ρ_d, and ρ_s are obtained in the similar way. For each iteration, all the components of each factor are updated in the order of D, F, G, ρ_d, and ρ_s. While the GAF G can be deduced from the NDF D, our method calculates the components of G independently of D for better fitting.

3.4 Principal Component Analysis of D and G

So far, we have represented the measured BRDF ρ_j with non-parametric factor representation for each wavelength. Fig. 3 visualizes the hemispherical distributions of NDF D and GAF G of *brushed_aluminium_1* material projected onto the unit disk. As shown in Fig. 3, D and G have similar distributions across different wavelengths. We further compress NDF D and GAF G across all the wavelengths by performing singular value decomposition:

$$D(\theta_h, \phi_h, \lambda) \approx \sum_k \sigma_k^D u_k^D(\theta_h, \phi_h) v_k^D(\lambda), \tag{11}$$

$$G(\theta, \phi, \lambda) \approx \sum_k \sigma_k^G u_k^G(\theta, \phi) v_k^G(\lambda), \tag{12}$$

where σ_k^D and σ_k^G are the k-th singular values for NDF D and GAF G, u_k^D and u_k^G are the k-th left singular vectors, and v_k^D and v_k^G are the k-th right singular vectors, respectively.

Fig. 4 shows the comparisons between the original NDF D and GAF G (λ = 689.9nm) and the reconstructed NDF and GAF using PCA with 99% cumulative contribution ratio of *green_pvc* material and *darth_vader_pants* material. As shown in Fig. 4, the reconstructed NDF and GAF match the original distributions well.

3.5 Importance sampling

Our method importance-samples the incident direction by sampling the half vector $\mathbf{h}$ based on NDF D. We first compute the average NDF $\bar{D}$ by integrating $D(\theta'_h, \phi_h, \lambda)$ as:

$$\bar{D}(\theta'_h, \phi_h) = \int y(\lambda) D(\theta'_h, \phi_h, \lambda) d\lambda, \tag{13}$$

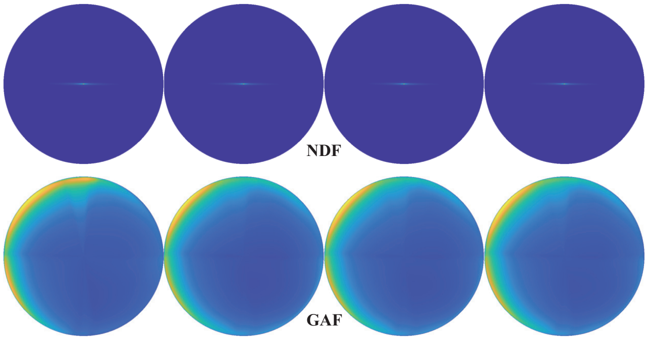

Figure 3: Visualization of NDF D (top) and GAF G (bottom) for *aniso_brushed_aluminium_1* (from left to right, 388.7nm, 489.2nm, 589.7nm, and 689.9nm). D and G show similar distributions across different wavelengths.

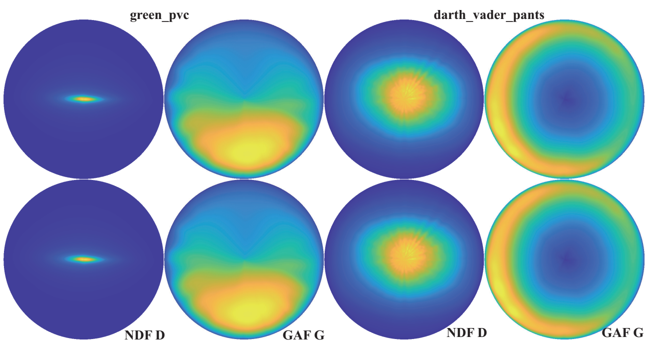

Figure 4: Visualization of original NDF D and GAF G (top), and those using PCA with 99% cumultive contribution ratio (bottom). The reconstructed NDF D and GAF G (bottom) can acculately recover the original distributions (top).

where y is the CIE_Y color matching function. Since $\bar{D}$ is a 2D table, we can sample from it straightforwardly using the alias method [35].

4 RESULTS

In this section, we first show the reconstruction accuracy of our non-parametric factor (NPF) representation model for measured anisotropic spectral BRDFs, then we show the rendering results of BRDFs edited using our method. The numbers of samples for θ'_h, ϕ_h, θ_d, and ϕ_d are 90, 180, 90, and 180, respectively. Those for θ and ϕ of GAF G are 90 and 180, respectively. The computational time to fit each anisotropic material is about six hours on a standard PC with Apple M1 Ultra 20 Core CPU. All images are rendered using HDR environment maps that are upsampled from RGB images to spectral ones using the method implemented in PBRT [27]. Details of the decomposed factors ρ_d, ρ_s, NDF D, Fresnel term F, and GAF G are shown in the supplemental material.

4.1 Non-Parametric Factor Representation

Fig. 5 shows the rendering results of the *Sphere* scene using anisotropic materials of the EPFL BRDF dataset [12]. We evaluate the visual quality of our representation using PSNR and SSIM shown in Fig. 5.

Table 2: The average PSNR, SSIM, data size, and average compression ratio of Fig. 5 with respect to the original data across all anisotropic materials of EPFL BRDF dataset.

	PSNR↑	SSIM↑	data size↓	ratio↓
NPF (w/o PCA of D/G)	45.08	0.9878	25.3MB	22.7%
NPF PCA (99%/99%)	44.93	0.9850	2.64MB	2.36%
NPF PCA (99%/95%)	44.45	0.9815	1.11MB	1.00%
NPF PCA (99%/90%)	43.87	0.9813	0.91MB	0.82%
NPF PCA (95%/95%)	43.83	0.9677	0.73MB	0.66%
NPF PCA (90%/90%)	42.60	0.9602	0.45MB	0.41%

The average PSNR, SSIM, average data size, and compression ratio of all (eleven) anisotropic materials in the EPFL BRDF dataset are shown in Table 2. As shown in Fig. 5, our NPF representation without PCA compression of NDF and GAF (Fig. 5(b)) can reproduce the visual appearance similar to the reference images (Fig. 5(a)) rendered by using the original measured anisotropic spectral BRDFs. Highly anisotropic materials, such as brushed_aluminium_1, metallic_paper materials, can be reproduced faithfully using our anisotropic NPF model. Since our method bases upon the microfacet model, materials that meet this assumption (e.g., metals like brushed_aluminium_1 and copper_sheet) can be represented with our NPF model. As shown in the insets of Fig. 5(b) of the visualization of relative mean square error (relMSE), the relative errors are slightly high at grazing angles, the same as the previous NPF method for isotropic BRDFs [2].

Fig. 5(c) shows the rendering results of our NPF representation using PCA-compressed NDF D and GAF G (with 99% cumulative contribution ratio). By exploiting the similarity of NDF D and GAF G in the spectral domain, the average data size is reduced to 1/10 (from 25.3MB to 2.64MB) using PCA, and the net compression ratio from the original EPFL BRDF (111.5MB) is 1/40. As shown in Figs. 5(b) and (c), all the rendering results using our NPF representation without PCA compression are indistinguishable from those using NPF with PCA compression, and the decreases in PSNR and SSIM between Fig. 5(b) and 5(c) are small (0.15 and 0.0028) as shown in Table 2. We also conducted experiments on the reconstruction accuracy of BRDFs with different cumulative ratios of PCA compression, 95% in Fig. 5(d), and 90% in Fig. 5(e). As shown in Figs. 5(d) and (e), most of the rendering results with PCA-compressed NDF D and GAF G provide high visual fidelity similar to those without PCA compression, and the decreases in PSNR and SSIM are still small (1.25 and 0.0201) on average (see Table 2), while the net compression ratio from the original BRDF is about 1/150. In the case of 90% cumulative contribution ratio, some materials (e.g., miro_7) can be rendered without losing accuracy compared with our NPF representation without PCA compression, and the net compression ratio is further reduced up to 1/333. However, other materials (e.g., copper_sheet) show degradation of visual quality, PSNR, and SSIM. In the following examples, NPF representation with both 99% cumulative contribution ratios for NDF D and GAF G is used unless otherwise stated.

Fig. 6 shows comparisons of the *Buddha* scene rendered with the original BRDF and our NPF representation using PCA-compressed NDF D and GAF G. While minor relative errors can be seen in contours of the Buddha model (i.e., grazing angles of incident and outgoing directions) as the Sphere scene, our NPF representation closely matches the original appearance as shown in Fig. 6 and visualized relMSE images. The average PSNR and SSIM of our method in Fig. 6 are 51.88 and 0.9984, respectively.

4.2 Comparison with neural-based method

Fig. 7 shows comparisons between our NPF representation (the cumulative contribution ratios for NDF D and GAF G are 99% and 95%) and Neural BRDF (NBRDF) [32], which is the only neural network representation method that can handle anisotropic materials. We follow the network architecture of NBRDF [32], except for the number of nodes in the output layer, to apply NBRDF to spectral BRDFs. We modified the author's code to encode anisotropic EPFL BRDFs with a $6 \times 21 \times 21 \times 195$ shape neural network. The average PSNR values of our method and NBRDF in Fig. 7 are 44.45 and 43.95, respectively. The average data sizes of our method and NBRDF are 1.1 MB and 26 KB, respectively. While NBRDF can represent anisotropic measured spectral BRDFs very compactly compared with our method, our method can reconstruct the original measured spectral BRDFs better than NBRDF in this case. In addition, our factored representation provides several editing tools, as described in Sec. 4.3, while NBRDF only accepts interpolating latent vectors to edit BRDFs.

We also compared our NPF representation with NBRDF in terms of computational performance, namely the computational time for BRDF evaluation and importance sampling. In our method, the computational time for BRDF evaluation depends on the number of truncated singular values to reconstruct NDF D and GAF G as shown in Eqs (11) and (12). The computational time for BRDF evaluation ranges from $1.156\mu s$ (brushed_steel_satin_pink material with three singular values for both D and G) to $2.742\mu s$ (satin_silk_2color material with 26 singular values for D and 6 for G). The average computational time for BRDF evaluation of our method is $1.898\mu s$, while that of NBRDF is $2.245\mu s$. Our BRDF evaluation is 18% faster than that of NBRDF since our BRDF evaluation is a simple look-up of low-dimensional tables.

For importance sampling, NBRDF uses Blinn-Phong BRDF whose parameters are inferred by inputting the latent vector of NBRDF into a shallow network. Then, the inverse cumulative distribution function (CDF) of Blinn-Phong BRDF is calculated for importance sampling. Extending this method to anisotropic BRDFs is difficult since anisotropic BRDFs lack the label data (parameters) for training. Therefore, we only measure the computational time for computing the inverse CDF under the assumption that the parameters are given, which is advantageous for NBRDF. The average computational time for importance sampling of our method is $0.0935\mu s$, while that of computing inverse CDF for NBRDF is $0.0678\mu s$. The total computational time of BRDF evaluation and importance sampling for our method is $1.99\mu s$, 16% faster than that for NBRDF ($2.31\mu s$).

For equal-memory comparison, we use a $6 \times 128 \times 256 \times 256 \times 195$ shape neural network whose data size is 660 KB, which is comparable to ours with 95% PCA (730KB). Using this network, the average PSNR value of NBRDF is 53.44 dB, which is 9.61 dB higher than ours as shown in Table 2. The use of a deeper network, however, also increases the time for BRDF evaluation ($78.41\mu s$), which is 41 times larger than ours. Therefore, our method seems to be suitable for applications that require fast evaluation speeds with moderate data size.

4.3 Editing Measured Spectral BRDFs

4.3.1 Editing NDF. Our NPF representation is capable of editing NDF directly. Our method edits NDF D using linear transformations [1, 15]. Fig. 8 shows the rendering results of the *Sphere* scene using edited BRDFs of copper_sheet material. The leftmost image of Fig. 8 shows the rendering result of our NPF representation (with PCA compression), and the edited NDF D and GAF G are shown at the bottom. By transforming D using the transformation matrix M, the specular highlight changes without changing other properties (e.g., the entire color), as shown in Fig. 8. This kind of material editing is difficult for interpolation-based editing of neural-based method that can change the whole appearance.

4.3.2 Editing diffuse colors. Our NPF representation allows the user to change the diffuse color by changing the diffuse coefficient ρ_d. To increase the number of expressible anisotropic spectral BRDFs without costly acquisition of surface reflectances of new materials, our method re-uses the measured data. To do this, our method represents 51 isotropic spectral materials in EPFL BRDF dataset with NPF representation and extracts ρ_d, ρ_s, D, F, and G.

Fig. 9 shows the rendering result of the *Pillow* scene. The former three pillows are rendered using edited darth_vader_pants material, and the two pillows in the back row are rendered using edited tarkin_tunic material. Our method replaces the diffuse coefficient of darth_vader_pants material with those of acrylic_felt isotropic materials as shown in Fig. 9. NDF D of the purple pillow is also edited to increase the anisotropy of darth_vader_pants material as shown in the inset. The diffuse colors of two pillows in the back row are also edited using those of acrylic_felt materials. NDF D of tarkin_tunic material is also edited to increase the specularity.

4.3.3 Editing specular colors. Our NPF representation also enables us to edit the specular colors by changing the specular coefficient ρ_s and Fresnel term $F(\theta_d, \lambda)$. Fig. 10 shows the rendering results of edited brushed_steel_satin_pink material, by replacing the specular color $\rho_s F$ with those of measured isotropic spectral BRDFs.

4.3.4 Editing Fresnel term. Our method allows the user to edit the extracted the Fresnel term F. Fig. 11 shows the editing of Fresnel term by adding iridescent effects. Fresnel term F is fitted with Airy reflectance [4] that considers the reflectance of a microfacet-surface coated with a single thin dielectric film (thickness d and refractive index η). The top row in Fig. 11 shows the rendering results of miso_7 material by adding a thin film of thickness $d = 615nm$ with varying refractive index η. By increasing the refractive index η, color fringes can be seen, especially for $\eta = 1.30$ and 1.50. The bottom row in Fig. 11 shows the rendering results with varying thicknesses. The change of the thickness d also changes the colors.

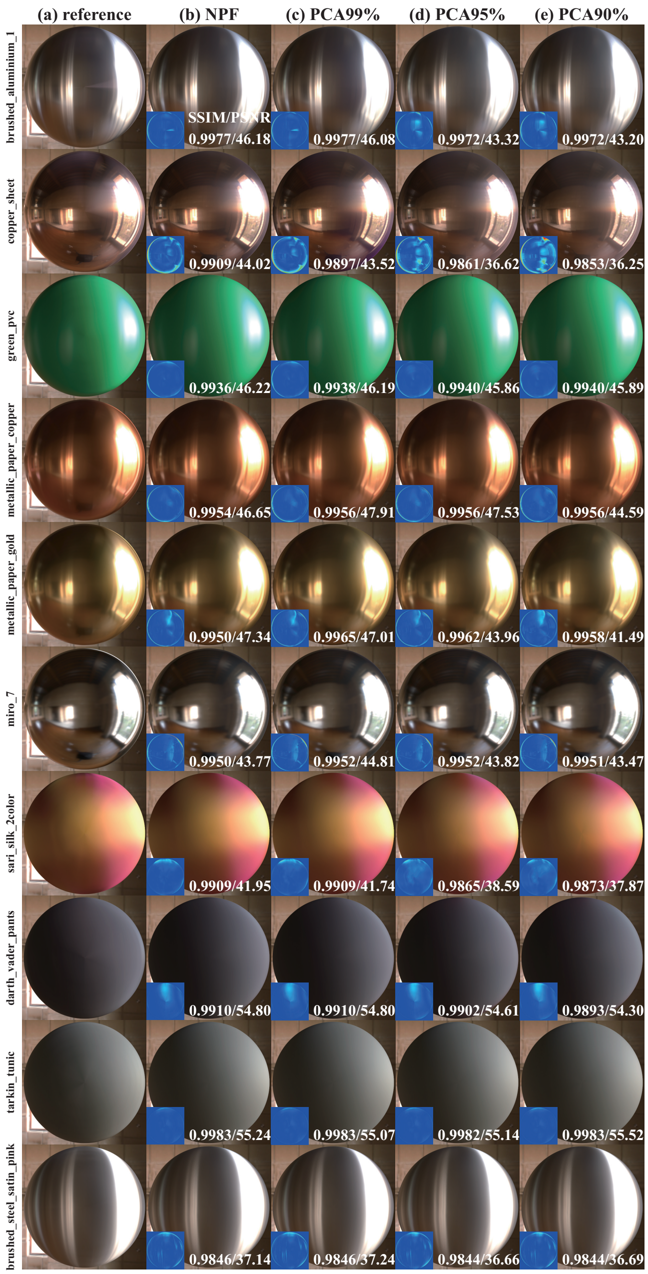

Figure 5: Rendering results of *Sphere* scene using our non-parametric factor representation (NPF): (a) reference (rendered with original EPFL BRDF), (b) NPF without PCA compression of NDF D and GAF G. (c)(d)(e) NPF with PCA compressed D and G whose cumulative contribution ratios are 99%, 95%, and 90%, respectively. The inset images visualize relative mean square errors (relMSE) where blue (red) colors indicate $0\%(\geq 5\%)$ relative errors. SSIM/PSNR are also shown in the bottom of relMSE images. The data size of (b) NPF (without PCA) is 25.3MB (the compression ratio is 22.7%), and that of (c) NPF with PCA 99% is 2.64MB (the compression ratio is 2.36%).

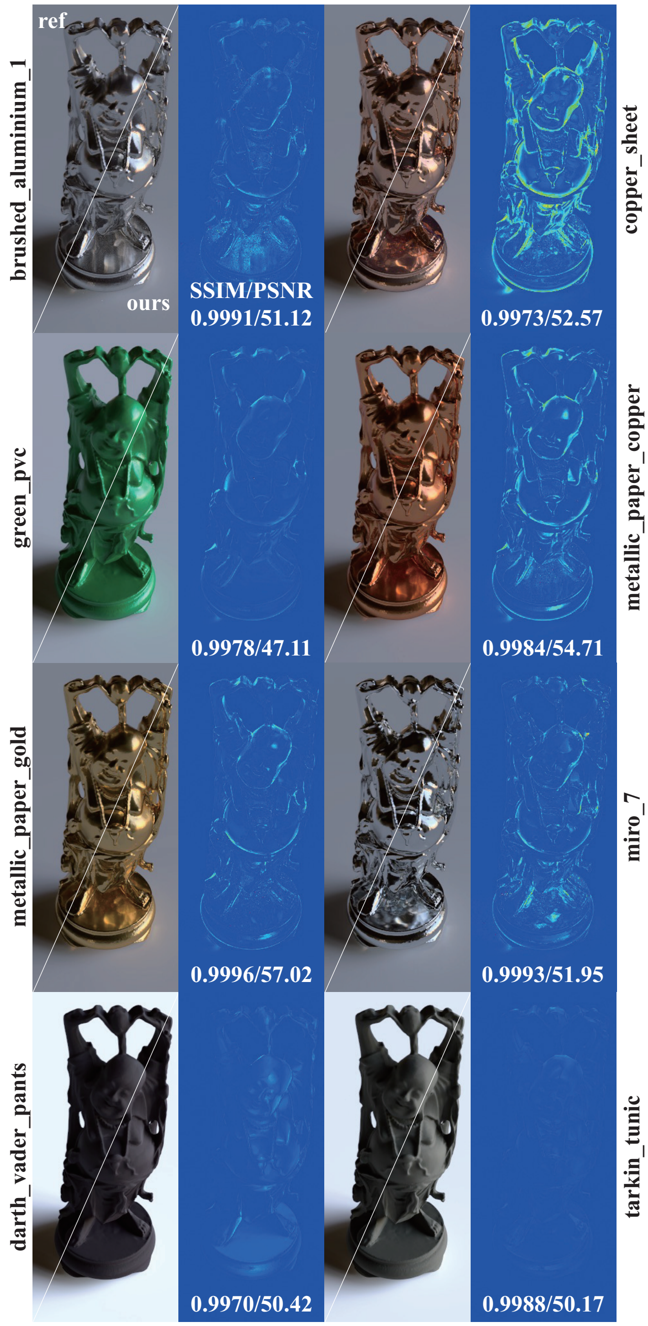

Figure 6: Comparison of Buddha scene rendered by using original EPFL BRDF and our method (PCA compression of NDF D and GAF G with 99% cumulative contribution ratio). SSIM and PNSR are shown in the bottom of each relMSE image. As shown in the comparisons and relMSE images, our non-parametric factor representation can provide visual fidelity similar to the reference.

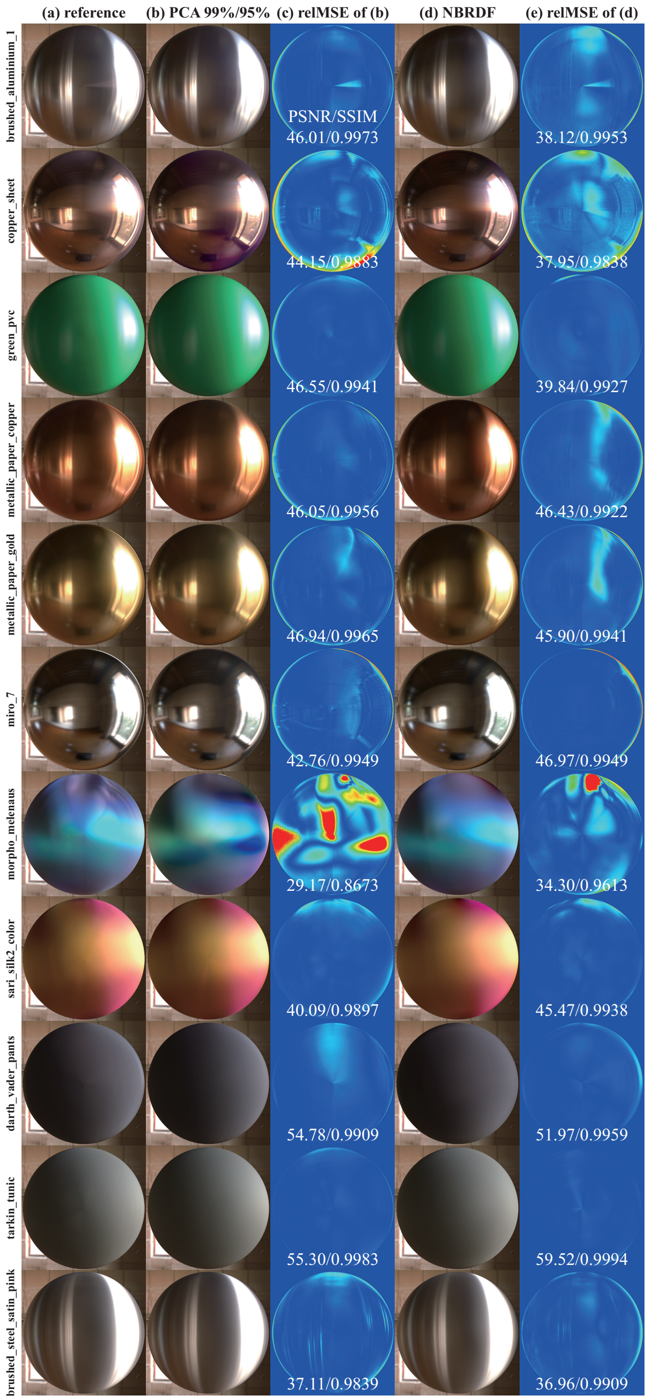

Figure 7: Comparison with Neural BRDF (NBRDF) [32]. The average PSNR values of our NPF representation with PCA-compression (99% for NDF D and 95% for GAF G) and NBRDF are 44.45 and 43.95, respectively.

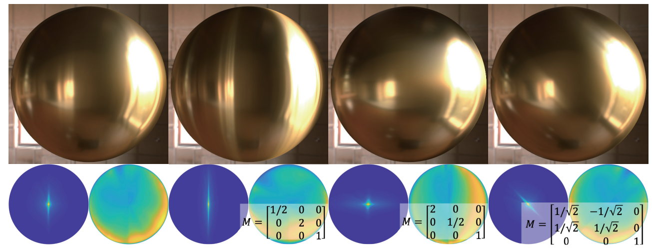

Figure 8: Editing NDF D by transforming D with transformation matrix M. The top row images are rendered by using the transformed NDF D (shown in bottom row). The leftmost image (copper_sheet material) is rendered using the original NDF D. The shapes of specular highlight are controlled by M (shown in the inset).

Figure 9: Editing diffuse colors ρ_d of *darth_vader_pants* material (front row three pillows) and *tarkin_tunic* material (back row two pillows). NDFs of the purple pillow and the yellow pillow are also edited (as shown in the insets) to increase the specularity.

Figure 10: Editing specular colors $\rho_s F$ of brushed_steel_satin_pink material by replacing those of isotropic materials (shown in the inset). Our method can change the specular colors without changing the shapes of highlights.

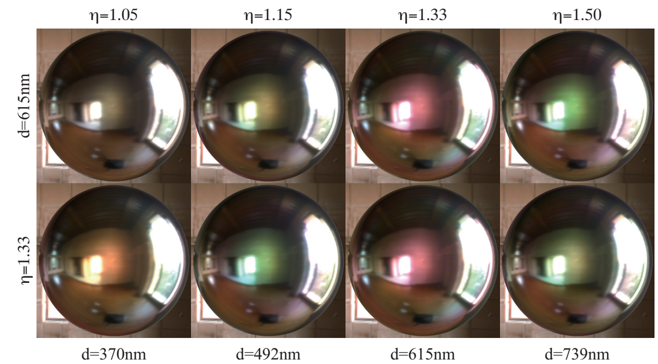

Figure 11: Editing iridescent effects by adding a thin film (refraction index η and film thickness d) on miro_7 material. By changing the refractive index η (top row) and the film thickness d (bottom row), our method can edit iridescent effects.

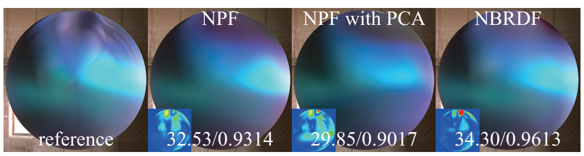

Figure 12: Failure case of our microfacet-based non-parametric factorization. ***morpho_melenaus*** **material exhibits complex reflections due to its mesostructure, which cannot be represented with neither microfacet models nor NBRDF.**

4.4 Limitations

While our method can represent most of the measured anisotropic spectral BRDFs, our method cannot represent anisotropic materials that deviate from the underlying microfacet theory. Fig. 12 shows the failure case of our NPF representation. While our NPF representation struggles to fit the complex anisotropic reflections, the high-frequency structural color variations arising from complex mesostructure of morpho_melanaus material cannot be represented as shown in Fig. 12.

5 CONCLUSION

We have proposed a non-parametric factor representation for measured anisotropic spectral BRDFs. Our method decomposes measured anisotropic spectral BRDFs into physically-based, meaningful factors such as diffuse/specular coefficients and NDF for compact representation. Our method further compresses the spectral domain of NDF and GAF, reducing the data size to 1/40 on average and up to 1/333. Our NPF representation also allows the user to intuitively edit measured anisotropic spectral BRDFs.

As for future work, we would like to investigate advanced fitting models that can deal with complex interactions of light beyond the microfacet theory, such as structural colors and diffraction of light. Currently, the proposed method is used for *forward* rendering. Applying our method to *inverse* rendering (e.g., predicting spectrum distributions of diffuse/specular coefficients from a single image) would be an interesting avenue for future work.

ACKNOWLEDGEMENT

This work was supported by JSPS KAKENHI Grant Numbers JP21H03571, JP21H05826, and JP23H03514.

REFERENCES

[1] A. Atanasov, V. Koylazov, R. Dimov, and A. Wilkie. 2022. Microsurface Transformations. *Computer Graphics Forum* 41, 4 (2022), 105–116.
[2] Mahdi M. Bagher, John Snyder, and Derek Nowrouzezahrai. 2016. A Non-Parametric Factor Microfacet Model for Isotropic BRDFs. *ACM Trans. Graph.* 35, 5 (2016), 159:1–159:16.
[3] M. M. Bagher, C. Soler, and N. Holzschuch. 2012. Accurate Fitting of Measured Reflectances using a Shifted Gamma Micro-facet Distribution. *Computer Graphics Forum* 31, 4 (2012), 1509–1518.
[4] Laurent Belcour and Pascal Barla. 2017. A Practical Extension to Microfacet Theory for the Modeling of Varying Iridescence. *ACM Trans. Graph.* 36, 4, Article 65 (2017), 14 pages.
[5] Alexis Benamira, Sachin Shah, and Sumanta Pattanaik. 2022. Interpretable Disentangled Parametrization of Measured BRDF with β-VAE. arXiv:2208.03914 [cs.GR]
[6] J. Bieron and P. Peers. 2020. An Adaptive BRDF Fitting Metric. *Computer Graphics Forum* 39, 4 (2020), 59–74.
[7] Ahmet Bilgili, Aydn Öztürk, and Murat Kurt. 2011. A General BRDF Representation Based on Tensor Decomposition. *Computer Graphics Forum* 30, 8 (2011), 2427–2439.
[8] James F. Blinn. 1977. Models of Light Reflection for Computer Synthesized Pictures. *SIGGRAPH Comput. Graph.* 11, 2 (1977), 192–198.
[9] Zhe Chen, Shohei Nobuhara, and Ko Nishino. 2022. Invertible Neural BRDF for Object Inverse Rendering. *IEEE Transactions on Pattern Analysis and Machine Intelligence* 44, 12 (2022), 9380–9395. https://doi.org/10.1109/TPAMI.2021.3129537
[10] R. L. Cook and K. E. Torrance. 1982. A Reflectance Model for Computer Graphics. *ACM Trans. Graph.* 1, 1 (1982), 7–24.
[11] Jonathan Dupuy, Eric Heitz, Jean-Claude Iehl, Pierre Poulin, and Victor Ostromoukhov. 2015. Extracting Microfacet-based BRDF Parameters from Arbitrary Materials with Power Iterations. *Computer Graphics Forum* 34, 4 (2015), 21–30.
[12] Jonathan Dupuy and Wenzel Jakob. 2018. An Adaptive Parameterization for Efficient Material Acquisition and Rendering. *ACM Trans. Graph.* 37, 6, Article 274 (2018), 14 pages.
[13] Jiahui Fan, Beibei Wang, Miloš Hašan, Jian Yang, and Ling-Qi Yan. 2022. Neural Layered BRDFs. In *ACM SIGGRAPH 2022 Conference Proceedings*. 4:1–4:8.
[14] J. Filip and R. Vávra. 2014. Template-Based Sampling of Anisotropic BRDFs. *Computer Graphics Forum* 33, 7 (2014), 91–99.
[15] Eric Heitz, Jonathan Dupuy, Stephen Hill, and David Neubelt. 2016. Real-Time Polygonal-Light Shading with Linearly Transformed Cosines. *ACM Trans. Graph.* 35, 4 (2016), 41:1–41:8.
[16] Nicolas Holzschuch and Romain Pacanowski. 2017. A Two-Scale Microfacet Reflectance Model Combining Reflection and Diffraction. *ACM Trans. Graph.* 36, 4, Article 66 (2017), 12 pages.
[17] Bingyang Hu, Jie Guo, Yanjun Chen, Mengtian Li, and Yanwen Guo. 2020. DeepBRDF: A Deep Representation for Manipulating Measured BRDF. *Computer Graphics Forum* 39, 2 (2020), 157–166.
[18] Jan Kautz and Michael D. McCool. 1999. Interactive Rendering with Arbitrary BRDFs using Separable Approximations. In *Rendering Techniques '99*. 247–260.
[19] Jason Lawrence, Aner Ben-Artzi, Christopher DeCoro, Wojciech Matusik, Hanspeter Pfister, Ravi Ramamoorthi, and Szymon Rusinkiewicz. 2006. Inverse Shade Trees for Non-Parametric Material Representation and Editing. *ACM Trans. Graph.* 25, 3 (2006), 735–745.
[20] Jason Lawrence, Szymon Rusinkiewicz, and Ravi Ramamoorthi. 2004. Efficient BRDF Importance Sampling Using a Factored Representation. *ACM Trans. Graph.* 23, 3 (2004), 496–505.
[21] Chen Liu, Michael Fischer, and Tobias Ritschel. 2023. Learning to Learn and Sample BRDFs. *Computer Graphics Forum (Proceedings of Eurographics)* 42, 2 (2023), 201–211.
[22] Joakim Löw, Joel Kronander, Anders Ynnerman, and Jonas Unger. 2012. BRDF Models for Accurate and Efficient Rendering of Glossy Surfaces. *ACM Trans. Graph.* 31, 1, Article 9 (2012), 14 pages.
[23] Wojciech Matusik, Hanspeter Pfister, Matt Brand, and Leonard McMillan. 2003. A Data-Driven Reflectance Model. *ACM Trans. Graph.* 22, 3 (2003), 759–769.
[24] Addy Ngan, Frédo Durand, and Wojciech Matusik. 2005. Experimental Analysis of BRDF Models. In *Proceedings of the Sixteenth Eurographics Conference on Rendering Techniques*. 117–126.
[25] Jannik Boll Nielsen, Henrik Wann Jensen, and Ravi Ramamoorthi. 2015. On Optimal, Minimal BRDF Sampling for Reflectance Acquisition. *ACM Trans.*

Graph. 34, 6, Article 186 (2015), 11 pages.

[26] Romain Pacanowski, Oliver Salazar Celis, Christophe Schlick, Xavier Granier, Pierre Poulin, and Annie Cuyt. 2012. Rational BRDF. *IEEE Transactions on Visualization and Computer Graphics* 18, 11 (2012), 1824–1835.

[27] Matt Pharr, Wenzel Jakob, and Greg Humphreys. 2016. *Physically Based Rendering: From Theory to Implementation (3rd ed.)* (3rd ed.). Morgan Kaufmann Publishers Inc., San Francisco, CA, USA. 1266 pages.

[28] Szymon M. Rusinkiewicz. 1998. A New Change of Variables for Efficient BRDF Representation. In *Rendering Techniques '98*. 11–22.

[29] Ana Serrano, Diego Gutierrez, Karol Myszkowski, Hans-Peter Seidel, and Belen Masia. 2016. An Intuitive Control Space for Material Appearance. *ACM Trans. Graph.* 35, 6 (2016), 186:1–186:12.

[30] Weiqi Shi, Zeyu Wang, Cyril Soler, and Holly Rushmeier. 2021. A Low-Dimensional Perceptual Space for Intuitive BRDF Editing. In *Eurographics Symposium on Rendering*, Adrien Bousseau and Morgan McGuire (Eds.). The Eurographics Association.

[31] Tiancheng Sun, Henrik Wann Jensen, and Ravi Ramamoorthi. 2018. Connecting Measured BRDFs to Analytic BRDFs by Data-Driven Diffuse-Specular Separation. *ACM Trans. Graph.* 37, 6, Article 273 (2018), 15 pages.

[32] Alejandro Sztrajman, Gilles Rainer, Tobias Ritschel, and Tim Weyrich. 2021. Neural BRDF Representation and Importance Sampling. *Computer Graphics Forum* 40, 6 (2021), 332–346.

[33] Tanaboon Tongbuasirilai, Jonas Unger, Christine Guillemot, and Ehsan Miandji. 2022. A Sparse Non-Parametric BRDF Model. *ACM Trans. Graph.* 41, 5 (2022), 181:1–181:18.

[34] Tanaboon Tongbuasirilai, Jonas Unger, Joel Kronander, and Murat Kurt. 2020. Compact and Intuitive Data-driven BRDF Models. *The Visual Computer* 36 (2020), 855–872.

[35] Alastair J. Walker. 1977. An Efficient Method for Generating Discrete Random Variables with General Distributions. *ACM Trans. Math. Softw.* 3, 3 (1977), 253––256.

[36] Chuankun Zheng, Ruzhang Zheng, Rui Wang, Shuang Zhao, and Hujun Bao. 2021. A Compact Representation of Measured BRDFs Using Neural Processes. *ACM Trans. Graph.* 41, 2 (2021), 14:1–14:15.

Received 20 February 2007; revised 12 March 2009; accepted 5 June 2009